Exchange coupling in the conical phase of Ho within Ho/Tb multilayers due to Ho magnetic sublattice disorder

Xiangshang Xiao,[1] Kunlong Zhao,[1] Yifan Cui,[1] Hanjun Liu,[1] Yi Wei,[1] Shuting Yang,[1] and Amitesh Paul[1,2,*]
[1]*Department of Materials Science and Engineering, and Guangdong Provincial Key Laboratory of Materials and Technologies for Energy Conversion, Guangdong Technion–Israel Institute of Technology, 241 Daxue Lu, Shantou, Guangdong 515063, China*
[2]*Department of Materials Science and Engineering, Technion–Israel Institute of Technology, Haifa 32000, Israel*

(Received 31 October 2023; revised 6 March 2024; accepted 22 April 2024; published 10 May 2024)

We explore the exchange bias coupling at the RE-RE interfaces (RE denotes rare earth) due to a plausible increase in the spin-imbalance induced by magnetic sublattice disorder around the temperature range where one of the REs exists in its conical phase while the other remains ferromagnetic (FM). In this regard, two highly textured multilayers with 29 monolayers (ML) of Ho are grown, which interface with 7 and 21 ML of Tb. For $ML_{Tb} = 7$, the noncollinear spin configuration constituting a fraction of the whole stack regulates the effect of the surface-area-to-volume ratio as the helix usually remains truncated, while for $ML_{Tb} = 21$, the helix can be sufficiently profound. Both samples exhibit at least two temperature-dependent phases of the spin configuration of Ho: conical and helical. For the $ML_{Tb} = 7$ sample, significant exchange bias fields of up to -0.57 ± 0.1 kOe are observed along with double hysteresis loops (DHLs) below 20 K. For $ML_{Tb} = 21$, the coupling strength diminishes to -0.055 ± 0.01 kOe as we also find shifts in the temperature behavior regimes related to the conical-to-helical and helical-to-paramagnetic phase fractions within Ho. This emblemizes the effect of helical phase formation in Tb on the Ho spin configuration. Instead of nanoclustering, regular FM behavior is seen around the temperature range of conical-to-helical phase evolution. As we replace 21 ML of Tb with 10 ML of a ferromagnet (CoFe), we find the usual DHLs and an exchange bias field up to -0.02 ± 0.01 kOe. The exchange bias phenomenon in Ho/Tb multilayer below 20 K is attributed to the small spin imbalance in the magnetic sublattice disorders in the conical phase of Ho.

DOI: 10.1103/PhysRevB.109.174422

I. INTRODUCTION

Information processing via the spin degree of freedom is an integral part of all-spin-based technology. Such processing is often influenced by several internal interactions, such as exchange, Ruderman-Kittel-Kasuya-Yosida (RKKY), or long-range dipolar interactions. Multilayers comprising either a combination of rare-earth (RE) and ferromagnetic (FM) materials (FM/RE) or two different RE materials (RE/RE) have been used to investigate topological domain configurations by exploiting their different (low-high) magnetic anisotropies. REs possess large orbital momentum, which leads to strong spin-orbit coupling. The associated larger magnetic anisotropy would therefore facilitate the magnetic modulations, which can propagate coherently over a long range aided by the RKKY interaction. The propagation can even be through the intervening layers, both nonmagnetic or magnetic.

The molecular beam epitaxial technique has been used to explore the effects of the artificial periodicity, finite layer thickness, and epitaxial strain affecting the long-range magnetic order within several RE-RE (Gd/Y, Dy/Y, Ho/Y, Er/Y, and Gd/Dy) superlattices (SLs) [1]. For RE-RE SLs systems (such as Ho/Y, Ho/Lu, Dy/Y, and Ho/Dy), the magnetic structural coherence was shown to extend over tens of nanometers and was due to similar Fermi surfaces, magnetic structures, and lattice constants, whereas for Ho/Er, for example, the coherence was revealed short-ranged due to the lack of such similarities [2,3]. The magnetic coherence across spacer layers was further found to depend on the band structure of the SL [4]. The turn angle per bilayer in the Ho blocks was found to change with temperature in Ho/Y SLs, which also influences the overall coherency [5]. In another study, the helical phase was found stable even under fields in Ho/Y SL higher than in the bulk [6]. Chirality in Ho/Y multilayers was explained in terms of the Dzyaloshinskii-Moriya interaction at the interfaces [7]. It was shown that the direction of the in-plane applied field can be used to modify the value and sign of the chirality parameter [8]. Dufour *et al.* investigated the link between structural and magnetic properties via magnetoelastic models [9]. Basal-plane ferromagnetic alignment of Tb moments within Tb blocks was reported to be coherent with a basal-plane helical ordering of Ho moments in Ho/Tb SLs as the coherence lengths extended over a few bilayers [10].

We have reported exchange bias fields within FM/RE or RE/RE multilayers. However, both interfacial layers in the multilayer stacks were essentially ferromagnetic. Thus a difference in their coercivities has essentially led to such a coupling. For example, in FM/RE (Fe/Tb [11,12] and Fe/Dy [13]) or RE/RE (Dy/Tb [14]), the exchange bias fields

*Corresponding author: amitesh.paul@gtiit.edu.cn

 ©2024 American Physical Society

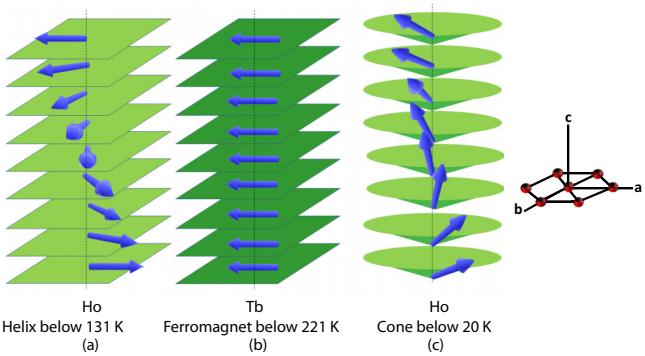

FIG. 1. Sketch of magnetic configuration in bulk. Sketch of the (a) basal plane helix of Ho, (b) ferromagnetic planes of Tb, and (c) cone phase of Ho with moments in bulk.

reported were around 1.0 kOe. The disappearance of the exchange bias fields around the temperature range of helical phases in Dy (80–180 K), Tb (229–221 K), and Er (20–52 K) was due to the small number of irreversible spins. The irreversible spins are responsible for exchange bias shift. The irreversible spins originated from the imbalance in the number of spins in each magnetic sublattice of the noncollinear structures [15]. However, an increase in the exchange bias field was recently reported in Er/Tb multilayers, and it occurs below 20 K where Er exists in a conical phase [16,17]. The small spin imbalance was seen to be overcome in the conical phase, where an increased magnetic sublattice disorder contributed to an increase in the exchange bias field of 0.17 kOe. Moreover, a superparamagnetic (SPM) or super-spin-glass (SSG) -like behavior was observed earlier in Fe/Tb, Fe/Dy, and Dy/Tb systems [11,13,14]. Such behaviors were attributed to spin-frustrated interfaces. On the contrary, typical FM behavior was reported for the Er/Tb system [16,17]. A similar sequence of conical and helical structures is also manifested in bulk Ho, which motivates us to investigate the exchange bias fields possibility within such highly textured multilayers. The observed saturation moments for Ho and Tb are $10.34\mu_B$ and $9.34\mu_B$, respectively [18].

A schematic of the basal plane helix, ferromagnet, and conical phase transformation of magnetic moments is shown in Figs. 1(a)–1(c) . Bulk Ho metal is a basal-plane helical antiferromagnet, which exists in between its Curie temperature of about 20 K and the Néel temperature of ∼131 K [18]. A magnetic field of around 1 T turns the helix into a helifan at around 50 K [19]. The helical structure consists of ferromagnetically ordered moments, which are in the basal planes of the hcp lattice. The moments in each plane are rotated by a certain angle with respect to the neighboring plane, thereby they form a helix along the crystallographic *c*-axis. The magnetic period is temperature-dependent with a length of about 10 monolayers (ML) at 40 K, decreasing with increasing temperature to about 7 ML at the Néel temperature (131 K). Below about 20 K, a cone is the stable phase in zero field, and the cone angle is almost independent of the applied field in the basal plane. At low temperatures, the hexagonal anisotropy being large, it forces the magnetic structure to be commensurable with the lattice.

For bulk Tb, on the other hand, the helical structure exists only between a small temperature range of 8 K (= 229–221 K), below which it orders ferromagnetically where the easy axis is along the *a*-axis. The interface area-to-volume ratio is expected to increase due to the truncated noncollinear spin configuration at the Tb interface for merely 7 atomic layers of Tb as the helical phase of Tb is expected to manifest more profoundly for 21 atomic layers. Note that the respective ordering temperatures are reported in bulk. In thin-film form, due to interface-induced modification in the coordination number, the volume to interface anisotropy and the fraction of the noncollinear spin configuration accommodated within the ordering temperatures are likely to change within the limited Ho and Tb layer thicknesses as they are expected to undergo anisotropic competition, as seen earlier in Er/Tb multilayers [20].

We explore two different thicknesses of one RE (Tb) while keeping the other RE thickness (Ho) fixed in Ho/Tb multilayers. The thickness dependence is expected to affect the noncollinear spin configuration constituting a fraction of the whole stack, regulating thereby the effect of surface area to volume ratio. The samples represent commensurable structures for different MLs, for example $ML_{Ho} = 29$ interfaced with $ML_{Tb} = 7$ and 21. Exchange-biased coupling is found to be negligibly weak for the Ho/Tb system for the temperature range where Ho possesses a noncollinear spin configuration or helical configuration. However, it becomes significant around the temperature where we expect the conical phase of Ho. Interestingly, here in Ho/Tb multilayers, we find an increased exchange bias field of 0.57 ± 0.1 kOe for the $ML_{Tb} = 7$ sample. For the $ML_{Tb} = 21$ sample, a decrease in the surface-area-to-volume ratio is expected, which in turn would affect the noncollinear spin configurations in Ho differently than for the $ML_{Tb} = 7$ sample. The exchange bias field reduces to -0.055 ± 0.01 kOe for the $ML_{Tb} = 21$ sample. Additionally, around the temperature range of conical-to-helical spin modulation of Ho, a typical FM behavior is observed via ac susceptibility measurements, particularly for $ML_{Tb} = 21$. Moderate exchange biased fields and double hysteresis loops (DHLs) are observed within a RE (Ho)-FM (CoFe) system with $ML_{CoFe} = 10$, as expected.

II. SAMPLES AND METHODS

A. Sample preparation

Magnetron sputtering (dc and rf) was used to prepare the samples on alumina (0001) substrates, of different compositions.

(i) Sample S1 [$Ho_{29}|Tb_7$]:
Nb(100.0 nm)/Y(100.0 nm)/[Ho(8.0 nm)/Tb(2.0 nm)]$_{\times N=10}$/TaN(2.0 nm).

(ii) Sample S2 [$Ho_{29}|Tb_{21}$]:
Nb(100.0 nm)/Y(100.0 nm)/[Ho(8.0 nm)/Tb(6.0 nm)]$_{\times N=10}$/TaN(2.0 nm).

(iii) Sample S3 [$Ho_{29}|CoFe_{10}$]:
Nb(100.0 nm)/Y(100.0 nm)/[Ho(8.0 nm)/CoFe(2.0 nm)]$_{\times N=10}$/TaN(2.0 nm).

Additionally, we grew two reference samples [Tb_{1230}]: Nb(50.0 nm)/Y(100.0 nm)/Tb(350.0 nm) and [Ho_{720}]:

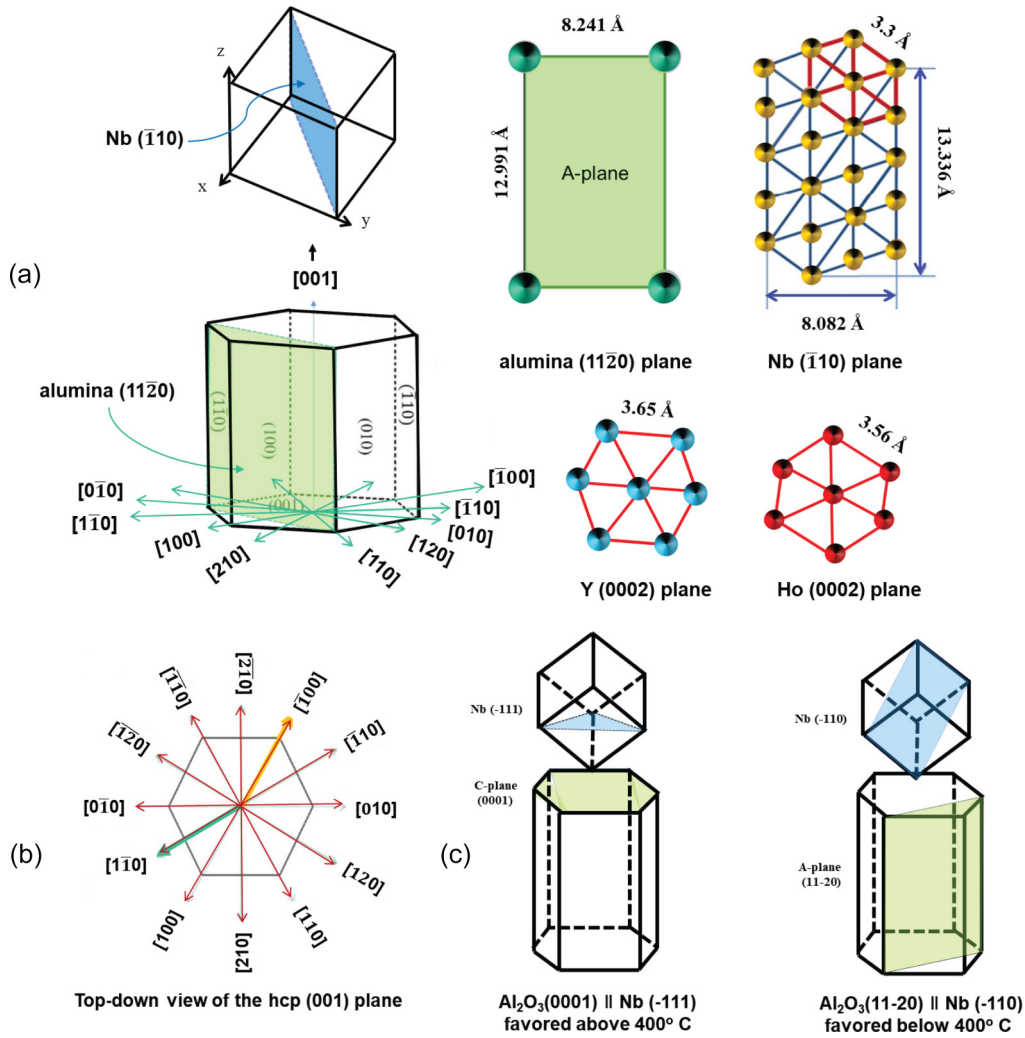

FIG. 2. Sketch of unit cells. (a) Sketch of a conventional hcp unit cell showing its close-packed planes and the labeled crystallographic directions. Shown alongside are the atomic spacings of the alumina (11$\bar{2}$0) plane, which shares a similar basis with the Nb ($\bar{1}$10), Nb with the Y (0002), and Y with the Ho (0002) planes. (b) Top-down view of the hcp (001) plane showing different directions relevant for the TEM images. The relevant directions [1$\bar{1}$0] and [$\bar{1}$00] are marked differently. (c) Three-dimensional relationships between the α-Al_2O_3 substrate and the Nb overlayer for two different planes of deposition.

Nb(100.0 nm)/Y(100.0 nm)/Ho(200.0 nm)/TaN(2.0 nm). Here, the number of ML is denoted by the subscripts in the sample names, and N designates the number of bilayers.

The Nb layer was grown on top of Al_2O_3 (alumina) as an effective buffer layer for the growth of RE films [21]. A unique epitaxial and three-dimensional relationship exists between the sapphire substrate and Nb, as alumina (0002) ∥ Nb ($\bar{1}$11), since the Nb ($\bar{1}$11) plane and the alumina (0002) plane (C-plane) share a similar basis. On the other hand, the sapphire (11$\bar{2}$0) plane (A-plane) shares a similar basis with the Nb ($\bar{1}$10), with the length of the sides equal to 8.241 and 12.991 Å for the former, and 8.082 and 13.336 Å for the latter, and it was confirmed earlier by experiments [22,23]. The combination of a sapphire plane (11$\bar{2}$0) substrate and the Nb (110) plane has been proven to be an effective seeding for the epitaxial growth of Y along its c-axis [22]. A schematic of the hcp crystallographic directions and the corresponding lattice spacings and three-dimensional unit cells are shown in Figs. 2(a) and 2(b) [22,23].

Figure 2(a) shows a comparison of the atomic spacing in the sapphire (11$\bar{2}$0) plane, the Nb (110) plane, and the Y (0002) plane. The Nb atoms in the (110) plane form a slightly distorted hexagon (marked in red), which matches closely to the hexagonal lattice in the Y (0002) plane. The in-plane axis of hcp Y is aligned with bcc Nb with 3:4 supercell commensuration in their nearest-neighbor distances along these axes. The initial growth of the Y (0002) lattice is strained, but the strain is relieved as the Y grows thicker. Therefore, a good hexagonal Y (0002) atomic plane can be achieved by depositing a thick Y seed layer before the RE/RE SL. A top-down view of the hcp (001) plane showing different directions is shown in Fig. 2(b).

Magnetron sputtering of RE structures on sapphire substrates was reported earlier [24]. According to Mašek *et al.* [25], in the range between 250 and 400 °C the (110) epitaxial orientation is favored, while for a substrate temperature higher than 400 °C the (111) epitaxial orientation takes place. In our case, we kept the deposition temperature at 320 °C [three-

dimensional relationships are shown in Fig. 2(c)]. When grown on top of Nb [$\bar{1}00$], the in-plane axis of hcp Tb or Ho [$10\bar{1}0$] usually suffers an elongation of the *c*-axis lattice parameter due to the initially strained Nb layer, strained by the alumina substrate. Adding a Y buffer layer between the Nb and Ho can cause an opposite effect, namely a contraction in the *c*-axis lattice parameter [26]. This effectively allows an almost unstrained growth of heteroepitaxial RE layers.

The substrates used were single-crystalline alumina (0001) wafers of 5×5 mm^2. The wafers were cleaned first in isopropyl alcohol and then ultrasonically in acetone and ethanol. They were mechanically clamped to a holder and were subsequently heated to 320 °C in vacuum for 20 min before deposition. The targets comprised disks of 2-in.-diam. The thicknesses of the targets were 0.25 in. for Ho (purity of 99.9%), 0.25 in. for Tb (purity of 99.9%), 0.055 in. for $Co_{80}Fe_{20}$ (purity of 99.95%), and 0.125 in. for TaN (purity of 99.5%). TaN was bonded to a copper backing plate. The targets were cleaned in an Ar atmosphere by presputtering for 1–5 min. We achieve a compromise between a high-quality crystal structure and a smooth surface for Tb and Ho (rms roughness $\approx$ 0.5 nm) by depositing at elevated substrate temperatures of 320 °C for all layers (including the buffer layers Nb and Y) except for the capping TaN layer, which was deposited at RT. The deposition rates were precalibrated (0.08 nm/s for Ho, 0.07 nm/s for CoFe, and 0.016 nm/s for Tb). The base pressure was maintained at 9.3×10^{-9} mbar while the Ar pressures in the magnetron sputtering chamber were 4×10^{-3} mbar during deposition.

B. X-ray

X-ray diffraction (XRD) and reflectometry (XRR) were performed using a Rigaku SmartLab (9 kW) diffractometer at the GTIIT laboratory equipped with a Cu (Cu $K\alpha 1 = 8.04$ keV) target.

C. Transmission electron microscopy

Specimen preparation for transmission electron microscopy (TEM) measurements was carried out using a ThermoFisher Talos F200X instrument at the Electron Microscopy Center (GTIIT). Sample preparation for the focused ion beam (FIB) was carried out using a Thermo Scientific Helios 5 DualBeam (SEM/FIB) system. Typical FIB procedures were applied for the TEM sample preparation in order to reduce the ion-beam-related sample's amorphous damage. Additionally, low voltages (5 and 2 kV) were used for the final polishing. High-resolution TEM (HRTEM) images were observed by using a ThermoFisher Talos F200X TEM, operated at 200 kV. A Ceta 16M camera 200 kV and Velox Imaging software were used to record the images. Using a ThermoFisher Talos F200X TEM, attached with a Super-X EDS Detector, energy dispersive x-ray spectroscopy (EDS) experiments were conducted. Data analysis for the FFT patterns was done using the Velox™ user interface module from ThermoFisher Scientific™ and plotted using the SingleCrystal™ software for different zone axes (ZAs).

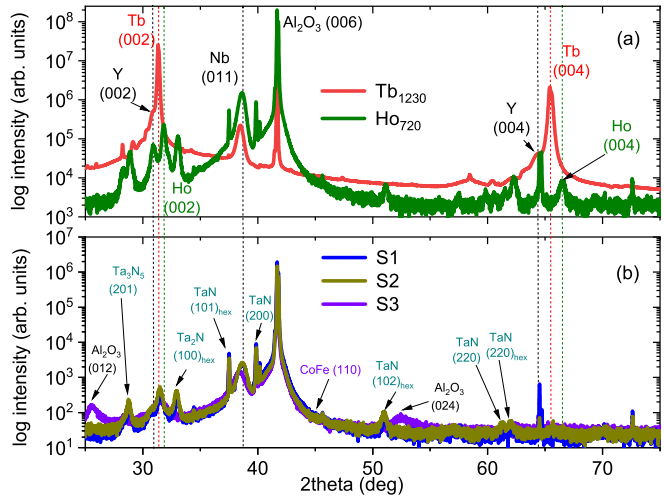

FIG. 3. XRD for *S*1–*S*3. (a) X-ray diffraction of the epitaxial thin films indicating the main structural peaks from films, buffers, and substrate for the two reference samples, Tb_{1230} and Ho_{720}. (b) The XRD peaks of highly textured multilayers *S*1, *S*2, and *S*3 are similar to that of single layers of Tb, Ho, and are indicated by the dashed lines. The peaks corresponding to the several polycrystalline phases of TaN-based compounds are also indicated.

D. Magnetometry

Conventional in-plane magnetizations were measured using a superconducting quantum interference device (SQUID) magnetometer from Quantum Design (MPMS3) at the Nanomagnetism and Advanced Scattering Techniques (Nam-AST) laboratory (Paul's Lab) within the GTIIT. The measurements were done at various temperatures and fields and different field cooling protocols. Conventional ac field susceptibility at various temperatures and frequencies was measured using an ac susceptibility module attached to the MPMS3.

III. RESULTS AND DISCUSSIONS

A. X-ray diffraction

Figure 3(a) shows the XRD profiles for the two reference samples, Tb_{1230} and Ho_{720}. The hex Ho (002) peak is seen at 31.81° while the hex Tb (002) peak is at 31.34° for the two reference samples. For $S1 - S3$, Fig. 3(b) shows (002) peaks corresponding to Ho or Tb as a combined peak at 31.48° instead of individual ones as the structure grows on similar templates. It also shows the buffer layer peaks corresponding to Y (002) at 30.66°, and the Nb (011) peak at 38.90°. *S*3, on the other hand, hardly shows the CoFe (110) peak, for example, due to its very low thickness (2.0 nm) and being mostly overshadowed by the TaN peaks.

Apart from the highly textured Tb, Ho, Nb, and Y peaks, the polycrystalline TaN capping layer peaks are visible at several angles. The peaks at 35.15°, 40.14°, and 59.63° can be identified as the (111), (200), and (220) planes of fcc TaN while the peaks at 28.83°, 33.34°, 37.91°, 51.02° and 59.60° can be identified as the (201) plane of Ta_3N_5, the (100) plane of hex Ta_2N, and (101), (102) and (220) planes of hex TaN.

Because of the total absence of any noticeable satellite peaks in the curves, there is no possibility to estimate the

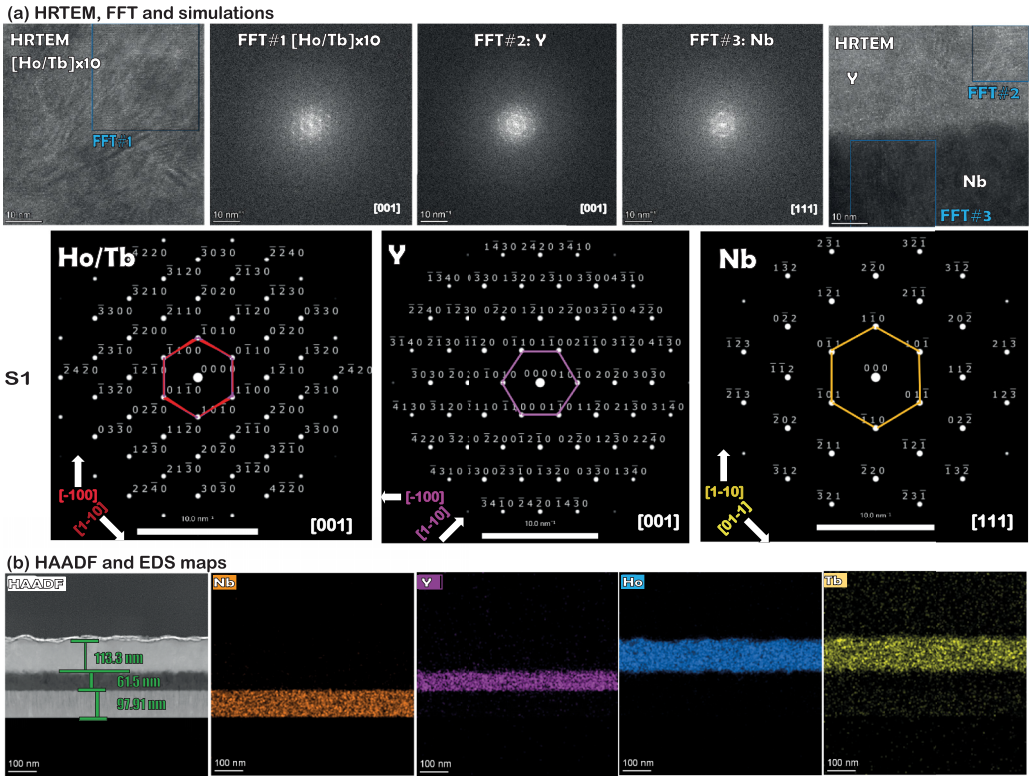

FIG. 4. HRTEM, FFT, simulations, and EDS for S1. (a) Cross-sectional HRTEM images of specimen $S1$, showing the layer sequence on alumina substrate. The corresponding FFT patterns of the area marked by the squares in the HRTEM images containing Nb/Y and Y/[Ho(8.0 nm)/Tb(2.0 nm)]$_{\times N=10}$ interfaces are also shown. Simulations for the FFT patterns for different zone axes: [001] for Ho, [001] for Y, and [111] for Nb are shown corresponding to the FFT patterns. The respective hexagonal spots (marked in pink), the hexagonal spots (marked in magenta), and the hexagonal spots (marked in yellow) corresponding to the multilayer, Y, and Nb are also depicted. (b) The HAADF STEM image along with the EDS maps of the elements Nb, Y, Ho, and Tb in the layer stack showing the interfaces.

coherence length. Since we kept the deposition temperature at 320 °C during the complete deposition time, it is expected to lose the out-of-plane structural coherency as the size of the crystallites is dependent on the orientation probability function and/or the spatial density [27]. Instead, real space microscopy imaging would indicate their structural coherency as investigated below.

B. Transmission electron microscopy

Figures 4(a) , 5(a), and 6(a) show the cross-sectional HRTEM images of $S1$, $S2$, and $S3$. One can readily see the abrupt interfaces between Nb, Y, and the multilayers with clear interface contrast. Fast Fourier transformation (FFT) patterns of the image concerning the area containing Nb/Y, $[Ho_{29}|Tb_7]_{10}$; Nb/Y, $[Ho_{29}|Tb_{21}]_{10}$; and Nb/Y, Y/$[Ho_{29}|CoFe_{10}]_{10}$ are also shown, as they are marked by the squares in the HRTEM images of Figs. 4(a), 5(a), and 6(a), respectively. FFT patterns show the diffraction spots for different ZA: [001] for Ho, [001] for Y, and [111] for Nb in $S1$ and $S2$ and also [001] for Ho/CoFe, [001] for Y, and [111] for Nb in $S3$. However, the CoFe layers in $S3$ are rendered noncrystalline since they have a different crystal structure. The simulations for the FFT patterns along different ZA for Ho, Y, and Nb in $S1$ and $S2$, and for Ho/CoFe, Y, and Nb in $S3$, are also shown.

The high-angle annual dark field scanning TEM (HAADF STEM) images of the interfaces in Figs. 4(b), 5(b), and 6(b) show the coherent interface features. HAADF image contrast is mainly related to the differences in atomic number Z and intensity varying as Z^2. Elemental identifications of Nb, Y, Ho, and Tb across the stack are shown in the corresponding EDS maps corresponding to $S1$ and $S2$. Similar elemental identifications of Nb, Y, Ho, and Co across the stack are shown in the EDS maps corresponding to $S3$. The HAADF STEM images show the out-of-plane grain size, which approximately matches the film thickness perpendicular to the film plane and extends up to ∼130–190 nm.

C. Magnetization measurements

1. Field hysteresis loops

Magnetic field hysteresis loops were measured in-plane at different temperatures for $S1$, $S2$, and $S3$ at various temperatures after field cooling in the presence of +70 kOe (7000 mT). Figures 7(a)–7(m), Figs. 8(a)–8(m), and Figs. 9(a)–9(l) show the hysteresis loops for $S1$, $S2$, and $S3$. The samples have saturation fields of 40–60 kOe. The two branches of the hysteresis loops, decreasing and increasing, give the respective remanent magnetization ($m_r = [m_r^+ - m_r^-]/2$), coercivity ($H_c = [H_c^+ - H_c^-]/2$), and exchange bias ($H_{eb} = [H_c^+ + H_c^-]/2$). The zoomed-in hysteresis loops at 2 K,30 K and 50 K,170 K ($S1$) are shown in Figs. 7(m) and

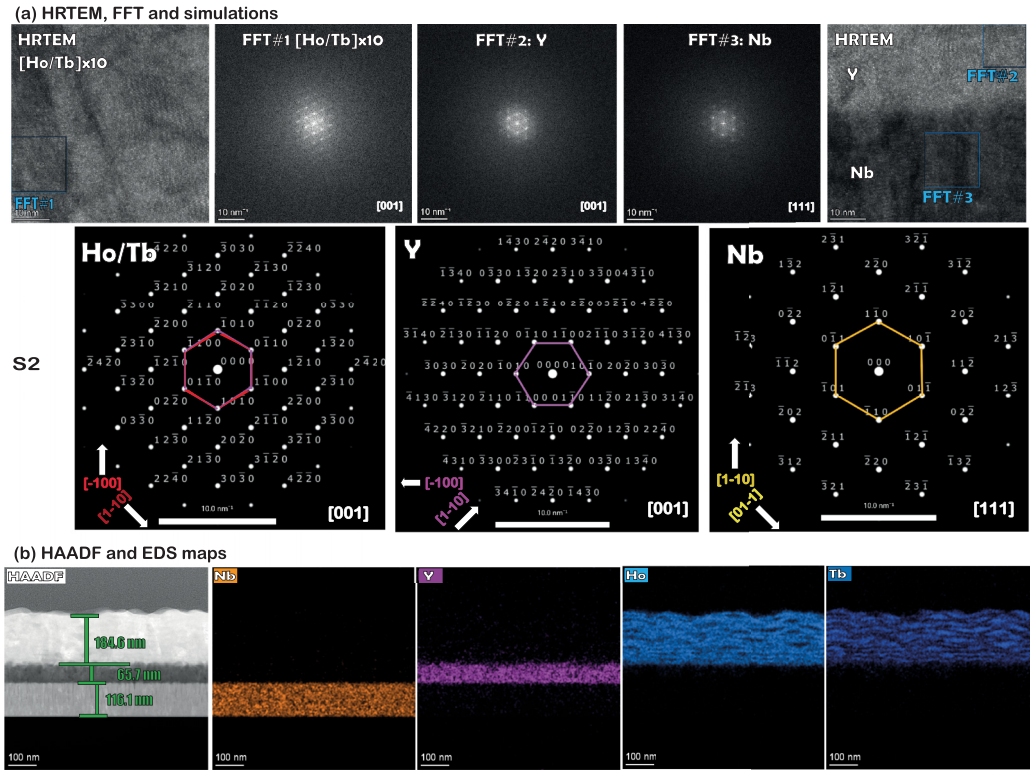

FIG. 5. HRTEM, FFT, simulations, and EDS for S2. (a) Cross-sectional HRTEM images of specimen $S1$, showing the layer sequence on alumina substrate. The corresponding FFT patterns of the area marked by the squares in the HRTEM images containing Nb/Y and Y/[Ho(8.0 nm)/Tb(6.0 nm)]$_{\times N=10}$ interfaces are also shown. Simulations for the FFT patterns for different zone axes: [001] for Ho, [001] for Y, and [111] for Nb are shown corresponding to the FFT patterns. The respective hexagonal spots (marked in pink), the hexagonal spots (marked in magenta), and the hexagonal spots (marked in yellow) corresponding to the multilayer, Y, and Nb are also depicted. (b) The HAADF STEM image along with the EDS maps of the elements Nb, Y, Ho, and Tb in the layer stack showing the interfaces.

7(n), at 30 K and 2 K,170 K ($S2$) in Figs. 8(m) and 8(n), and at 2 K, 20 K, 50 K and 100 K,170 K ($S3$) in Figs. 9(m) and 9(n) within the limited field ranges.

We see similar shifts for the bottom half (top half) along the decreasing (increasing) branch of the loops. We categorize such hysteresis loops in terms of the superimposition of two-loops: The first one is called the primary loop, centered around 0.0 Oe along the x-axis. The second one is called the secondary loop, which has its center shifted horizontally along the x-axis, along the positive as well as negative directions. $H_c^{\pm(p)}$ (primary loop) is the coercivity associated with the values where the magnetization $M = 0$. However, this is not true for $H_c^{\pm(s1,s2)}$ (secondary loops). The $H_c^{\pm(s1,s2)}$ of the secondary loops is derived from the centers of the subloops. The secondary loops are perceived as two symmetric loops superimposed on the primary loop on both sides of the field axis. This happens when the system is broken into a bidomain state, i.e., oppositely biased subsystems with equal magnitudes of exchange bias acting on the FM (here the FM is Tb below 221 K). Such a superposition of two loops (primary and secondary) has been reported for Fe/Tb [11] and also in Fe/Dy [13] systems, and it was coined a "double hysteresis loop" (DHL). Oppositely biased subsystems with equal magnitudes of exchange bias acting on the DHLs are expected to be symmetric. DHLs are seen between 2 and 100 K in $S1$ [Fig. 7(n)], and between 20 and 300 K in $S3$ [Figs. 9(m) and 9(n)]. No identifiable DHL can be found in $S2$ [Figs. 8(m) and 8(n)]. Notably, the DHLs in $S3$ [Fig. 9(n)] are the most prominent ones as CoFe remains FM below RT, leading to stronger coupling.

We did not find the center of the secondary loop shifted along the y-axis. For $S1$, viz., at 50 K [Fig. 7(n)] the centers of the secondary loops are marked by two dotted lines corresponding to both subsystems at the bottom and upper halves. The blue arrows mark the coercive fields for the bottom half and top half of the hysteresis loop. The shaded regions in gray mark the equal proportions of the two subsystems along the y-axis extending down from their saturation states at $\pm 1.55\mu_B$/per atom to $\pm 0.93\mu_B$/per atom. The later moment values are at the centers of the secondary loops and are symmetric in both halves—the top loop-shift ($+0.93\mu_B$/per atom) and the bottom loop-shift ($-0.93\mu_B$/per atom)—designating the respective coercive fields. The red arrows mark the coercive fields of the primary loop. Since the coercive fields of the primary loops are temperature-dependent, so are the coercive fields for the secondary loops. The magnetization values used for the centers of the secondary loops are different for each hysteresis loop at various temperature and thereby for each sample. To clarify furthermore, Fig. 10 explicitly shows the primary and the two secondary hysteresis loops representing the bidomain states as dotted lines with different colors, which are superimposed in forming the loop of $S1$ at 50 K.

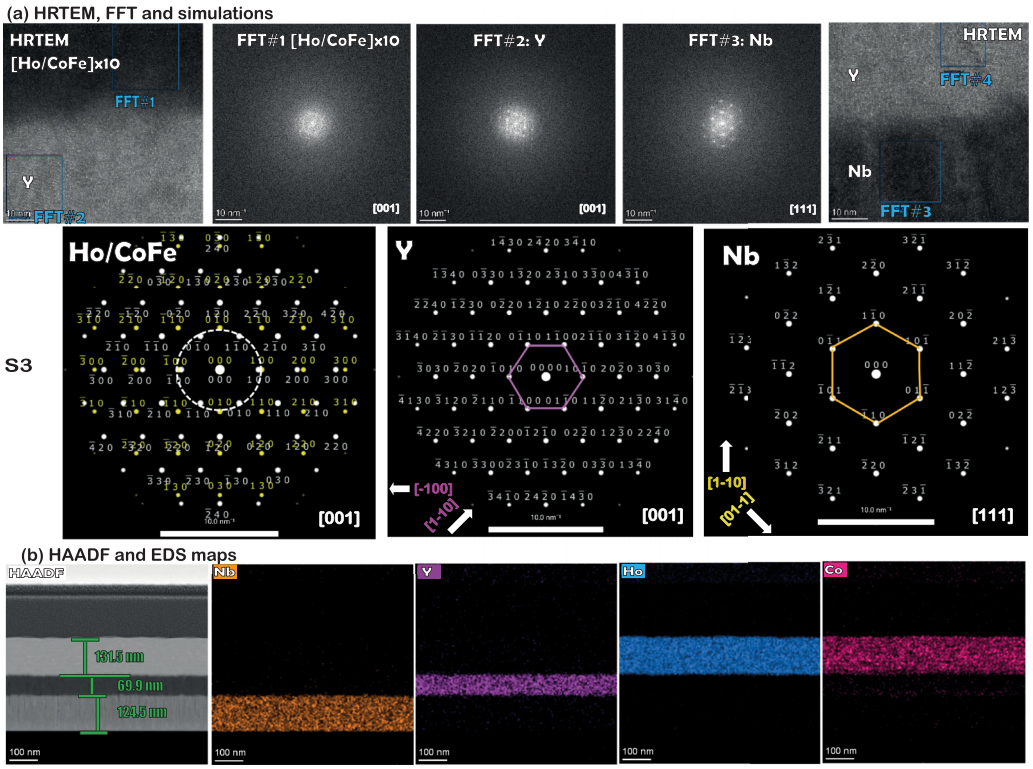

FIG. 6. HRTEM, FFT, simulations, and EDS for $S3$. (a) Cross-sectional HRTEM images of specimen $S3$, showing the layer sequence on alumina substrate. The corresponding FFT patterns of the area marked by the squares in the HRTEM images containing Nb/Y and Y/[Ho(8.0 nm)/CoFe(2.0 nm)]$_{\times N=10}$ interfaces are also shown. Simulations for the FFT patterns for different zone axes: [001] for Ho, [001] for Y, and [111] for Nb are shown corresponding to the FFT patterns. The respective hexagonal and rectangular spots (marked in white circle), the hexagonal spots (marked in magenta), and the hexagonal spots (marked in yellow) corresponding to the multilayer, Y, and Nb are also depicted. (b) The HAADF STEM image along with the EDS maps of the elements Nb, Y, Ho, and Co in the layer stack showing the interfaces.

The loops at 2 K in $S1$ are marked by saw-tooth-like steps along the decreasing and increasing branches of the loop in [Fig. 7(a)]. The steplike feature usually appears for very high-quality growth. Such saw-tooth-like steps have been reported earlier [16,17]. The steps can originate from three transition regions between the canted-ferromagnetic and spin-flop processes, and they were found to be dominated by degenerate bidirectional fluctuations due to competing anisotropies, which are expected within a conical phase [28,29]. The cases of spin-flop across the zero field at 2 K are most evident.

The variations of m_r and the monotonic decrease of H_c and H_{eb} with increasing T are plotted for $S1$, $S2$, and $S3$ in Figs. 11(a), 12(a), and 13(a). Both m_r and H_c go to zero at $T = 125$ K for $S1$ and $T = 200$ K for $S2$, relevant for the primary loops. The temperature where $H_{eb} \rightarrow 0$ signifies an apparent blocking/freezing temperature of the Ho/Tb magnetically coupled system. For $S3$, neither H_c nor m_r ever goes to zero. This indicates a non-SPM/SSG (blocking/freezing) behavior.

At temperatures below 20 K where the Ho layer is supposed to remain in a conical phase (marked in lime), we find a maximum $H^1_{eb} = -0.57 \pm 0.01$ kOe at 2 K from the primary loop [Fig. 11(b)] and a maximum $H^2_{eb} = \pm 11.0 \pm 1$ kOe at 100 K from the secondary loop [Fig. 11(c)] for $S1$. Below 50 K, H^2_{eb} could not be properly estimated except at 2 K ($\pm 3.5 \pm 0.5$ kOe).

For $S2$, $H^1_{eb} = -0.055 \pm 0.005$ kOe at 2 K [Fig. 12(b)] and was found oscillating its sign with increasing temperature reaching a maximum of $H^1_{eb} = -0.016 \pm 0.005$ kOe at 130 K before dying out at 250 K [Fig. 12(c)]. Below 20 K, Ho is expected to be in its conical phase, and around the temperature range between 20 and 131 K, a helical spin configuration is expected, above which negligible exchange bias fields can be seen, signifying a very weak coupling between Ho and Tb. No H^2_{eb} can be seen for $S2$, nor was one observed in Er/Tb multilayers, which possess similar thicknesses ($ML_{Er} = 21$; $ML_{Tb} = 21$) of individual layers [17]. When an interface monolayer reconstructs into a sufficiently rigid canted moments configuration [30], which is a highly plausible scenario for the conical phase of Ho, the coupling phenomenon as a function of temperature results in uncertainty during each field cooling process contributing to the spin imbalance in each magnetic conical sublattice disorder [15]. Since the overall spin imbalance in Ho is evidently higher than in Er, a higher H^1_{eb} is expected below 20 K (where a conical phase is expected) and also for a higher temperature range (where a helical phase is expected).

A maximum $H^1_{eb} = -0.02 \pm 0.005$ kOe at 2 K [Fig. 13(b)] and a maximum $H^2_{eb} = \pm 10.7 \pm 0.1$ kOe at 30 K are seen for $S3$ [Fig. 13(c)]. The higher values of H^2_{eb} than in Er/CoFe ($\pm 0.35 \pm 0.02$ kOe) [17] can be attributed to a stronger coupling between helical RE (Ho) and FM (CoFe) and also to the

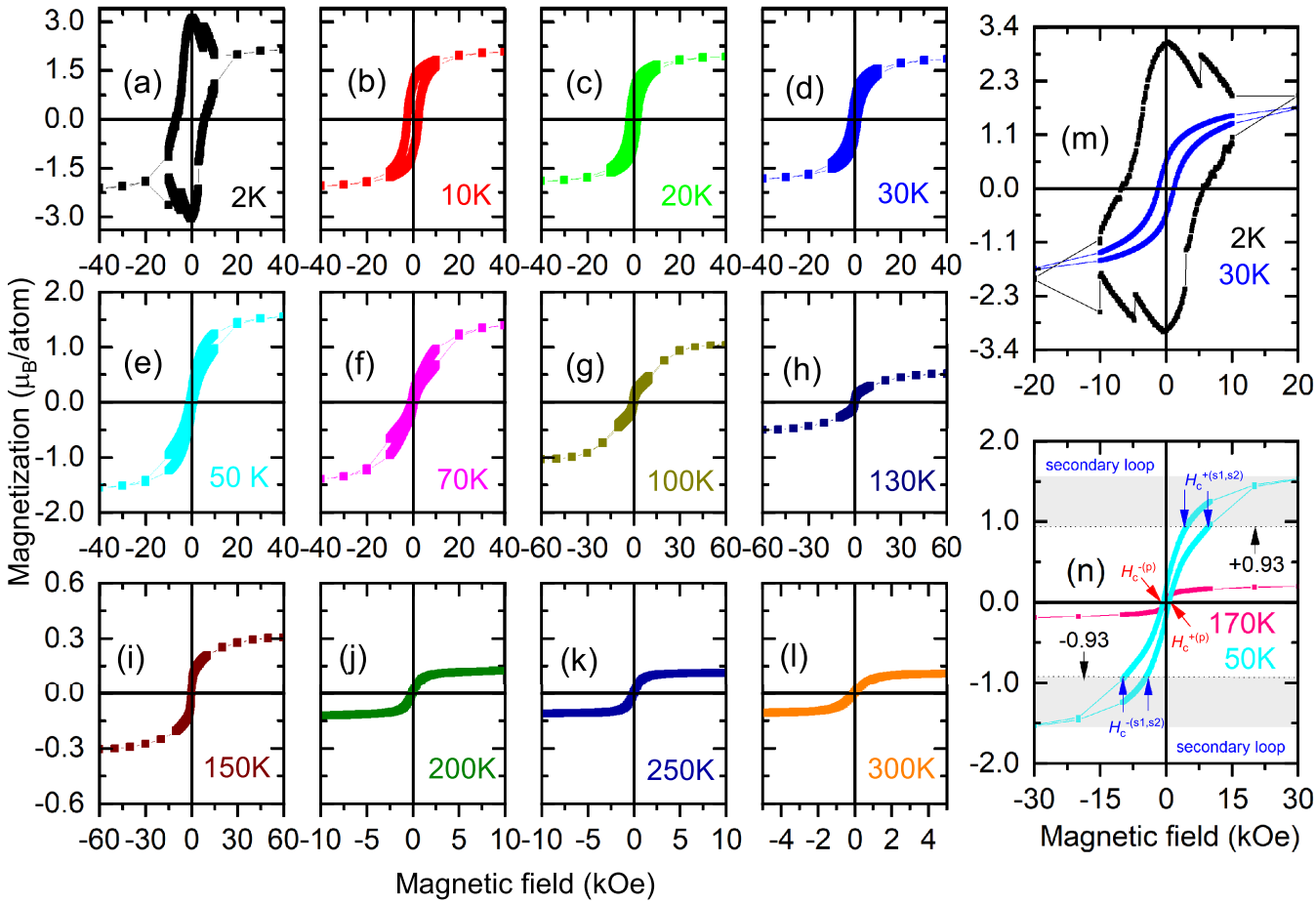

FIG. 7. Hysteresis loops for $S1$. (a)–(l) Hysteresis loops at various temperatures showing different shifts of the loops with temperature after field cooling. (m),(n) Zoomed-in plots of the loop shifts rendering $H_{eb}^{-/+}$ values at 2 K (saw-toothed DHL), 30 K and 50 K (DHL), and 170 K. The blue arrows indicate the two coercive fields $H_c^{-(s1,s2)}$ at the bottom half and the other two $H_c^{+(s1,s2)}$ at the top half of the secondary loops concerning the DHL at 50 K, while the red arrows indicate the two coercive fields $H_c^{\pm(p)}$ of the primary loop. Proportions of the two subsystems extended along the y-axis are shown by the shaded gray regions at the top and down halves.

lower FM thickness (10 MLs) in Ho/Tb instead of 30 MLs in Er/Tb.

Both m_r as well as H_c indicate relaxation and magnetic irreversibility for $T < T_F$, typical for supermagnetic blocked or frozen spin-clusters [31]. Here, T_F is the blocking/freezing temperature. By applying an external field, the energy barrier against the anisotropy appropriate for SPM/SSG relaxation can be reduced. At a certain magnetic field, which is the coercive field, the magnetization can be made to effectively disappear and is given by

$$H_c = 2\frac{K_u}{m_s}\left[1 - \left(\frac{T}{T_F}\right)^{\frac{1}{\alpha}}\right] \quad (1)$$

for an ensemble of noninteracting clusters of spins (SPM), where K_u is the anisotropy constant, m_s the saturation magnetization, and $\alpha = 2$ [32].

The H_c versus $T^{1/2}$ plot in the inset of Fig. 11(a) shows a linear behavior for $S1$. The respective temperature where H_c cuts the $T^{1/2}$ axis is given by the corresponding blocking or freezing temperatures $T_{F1}(0) = 25$ K and $T_{F2}(0) = 100$ K in $S1$, while $T_{F1}(0) = 56$ K and $T_{F2}(0) = 205$ K in $S2$ [Fig. 12(c)]. Between 30–72 K = 42 K (= ΔR_{S2}), one finds a transitional regime in $S2$ [16]. Note that $\Delta R_{S1} = 0$, which indicates the effect of increased Tb thickness in $S2$ in the FM phase. A linear behavior can be a signature of the SPM/SSG type of spin-clustering, while a nonlinear behavior generally indicates an SSG type of spin-clustering in case both m_r and H_c go to zero. One may note that Tb is ferromagnetic below 221 K, and in the temperature range between 20 and 131 K, one expects a helical spin configuration of Ho. Thus, the linear regions in the H_c versus $T^{1/2}$ plots indicate an apparent nanoclustering or a regular FM behavior. However, the $T^{1/2}$ plots alone cannot discern the two behaviors, SPM/SSG.

As expected, the H_c versus $T^{1/2}$ plots in the inset Fig. 13(a) show a nonlinear behavior for $S3$. Such a nonlinear behavior indicates a regular FM, which is obviously due to the presence of CoFe, instead of Tb in $S1$ or $S2$.

To clarify the two regimes associated with two freezing temperatures, we show the log-log scale plots of H_c versus $T^{1/2}$, H_c versus T, and their first derivatives $d(H_c)/dT^{1/2}$ versus $T^{1/2}$ for $S1$ and $S2$ in Figs. 14(a)–14(f). We also show the simulated curves for three α values for two different sets of $T_F(0)$ values for each sample in Figs. 14(a), 14(b), 14(d), and 14(e). The simulations confirm the existence of

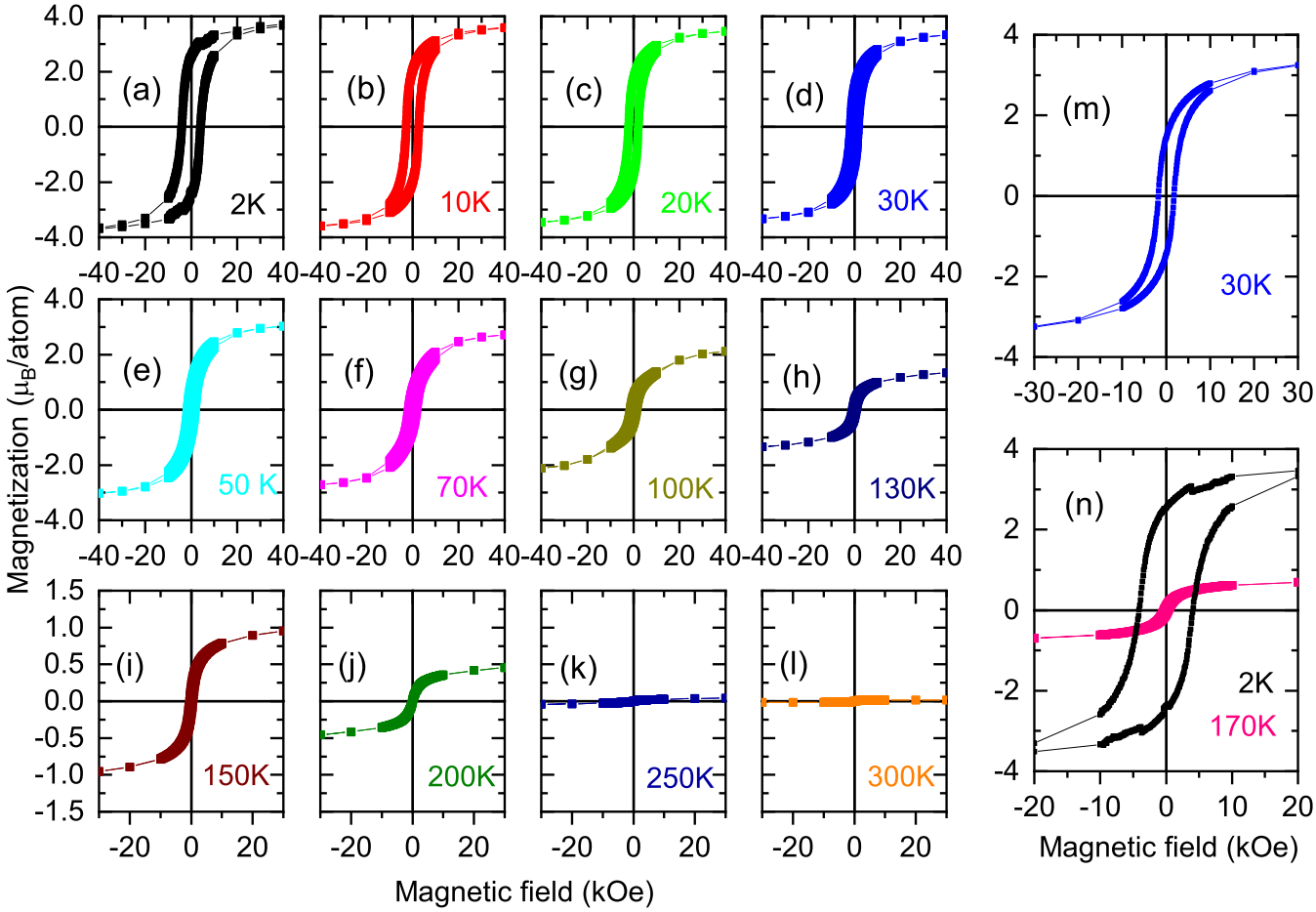

FIG. 8. Hysteresis loops for S2. (a)–(l) Hysteresis loops at various temperatures showing different shifts of the loops with temperature after field cooling. (m),(n) Zoomed-in plots of the loop shifts rendering $H_{eb}^{-/+}$ values at 30 K and 2 K, 170 K.

two regimes, which match best with a different set of normalization factors employed for the two regimes where the exponent factor $\alpha = 2$ is the same [31]. Furthermore, both sets of derivative plots clearly show the points of inflection for the curves, confirming again the existence of the two regimes in each sample [Figs. 14(c) and 14(f)]. Our inference is also in accordance with our previous findings in similar Er/Tb multilayer systems [16]. Nonetheless, one may note that the assessment of the two regimes is tenuous given the limited number of data points below 5 K, particularly in $S1$, which can be due to the small Tb thickness.

It may be noted that there exist two different nanoclustering behaviors within two different temperature regimes (r^1 and r^2), which barely evolve with the increase in thicknesses of Tb ($d_{Tb} = 2.0$ and 6.0 nm). This is because of the fact that Tb remains ferromagnetic below 221 K. For example, for $S1$, the linear behaviors are between 0–16 K (r_{S1}^1) (where the curve deviates from linearity) and 16–100 K (r_{S1}^2) (where the curve intercepts the x-axis). For $S2$, they are between 0–56 K (r_{S2}^1) and 69–205 K (r_{S2}^2). Thus, as we go from $ML_{Tb} = 7$ to $ML_{Tb} = 21$, the first ranges are $\Delta r_{S1}^1 = 16$ K and $\Delta r_{S2}^1 = 56$ K as the limit changes from 16 to 56 K while the second ranges are $\Delta r_{S1}^2 = 84$ K and $\Delta r_{S2}^2 = 136$ K as the limit changes from 100 to 205 K. These shifts can therefore be related to the higher Tb layer thickness in $S2$ affecting the temperature regimes of the two magnetic phases in Ho more effectively.

The H_{eb}^1 values are found fluctuating, going from positive to negative (or negative to positive) values for $S2$ and $S3$, which stems from the respective antiferromagnetic (or ferromagnetic) coupling at the Ho/Tb interfaces during field cooling. Positive or negative exchange bias may occur when an antiferromagnetic interface monolayer reconstructs into a sufficiently rigid canted moment configuration [30], a highly plausible scenario for the conical phase of Ho. Thus, the fluctuating coupling as a function of temperature in $S1 - S3$ results from the uncertainty in the small-imbalance for the number of spins in each magnetic conical and helical sublattice disorder during each field-cooling protocol [15].

2. Field-cooled and zero-field-cooled measurements

Characterizations of the magnetic properties were done using the field-dependent magnetization (M) measurements as a function of temperature (T) using standard field-cooled (FC) and zero-field-cooled (ZFC) protocols. We applied different magnetic fields $\mathbf{H}_a = 10$ Oe (1 mT) to 1000 Oe (100 mT) for $S1$, $S2$, and $S3$ during measurements after cooling down to 2 K in the presence of $\mathbf{H}_a = 70$ kOe/7000 mT (FC). The same protocol was used when the samples were cooled down to 2 K

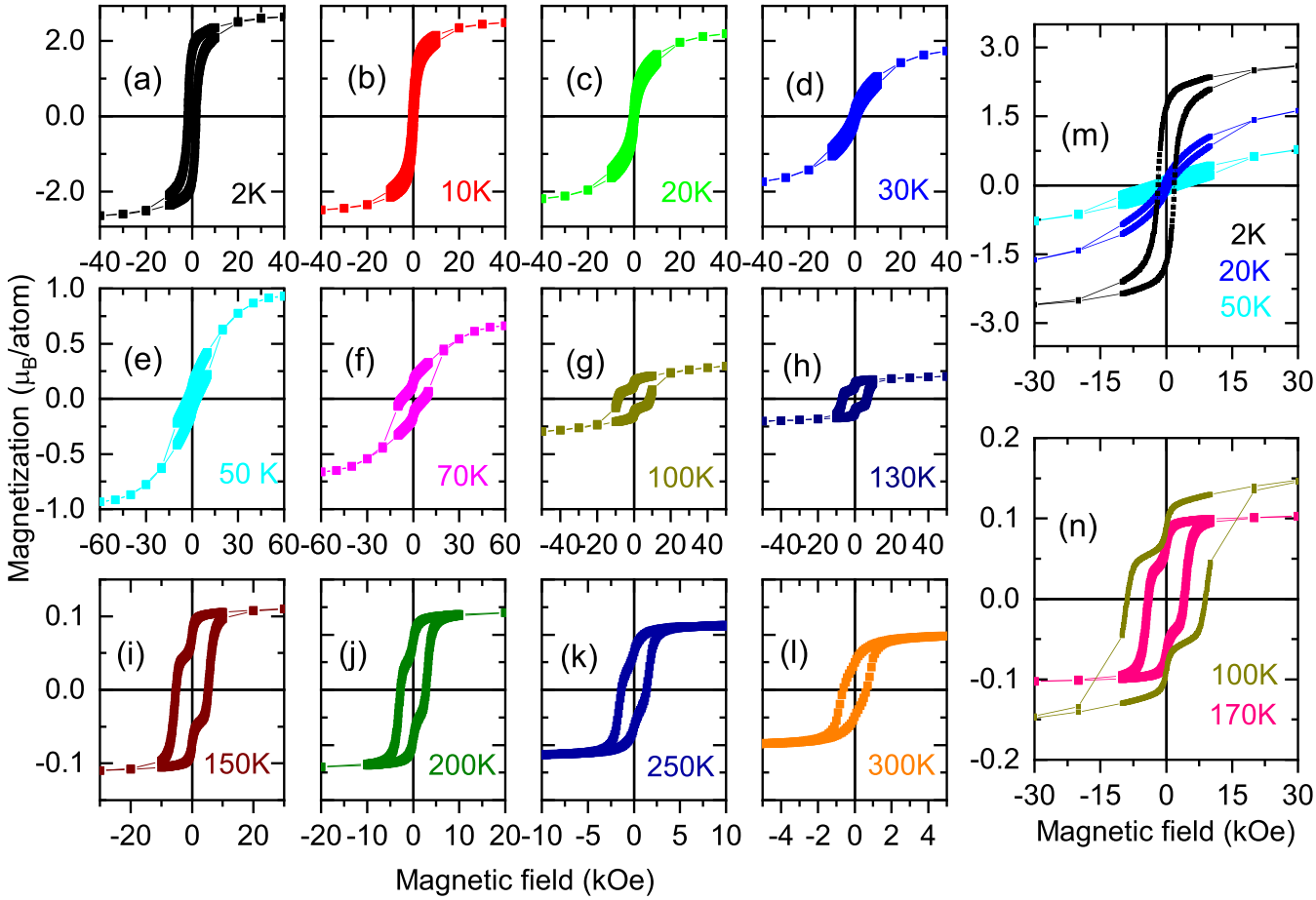

FIG. 9. Hysteresis loops for S3. (a)–(l) Hysteresis loops at various temperatures with temperature after field cooling. (m),(n) Zoomed-in plots of the loop shifts rendering $H_{eb}^{-/+}$ values at 2 K, 20 K, 50 K, and 100 K (DHL), and 170 K (DHL).

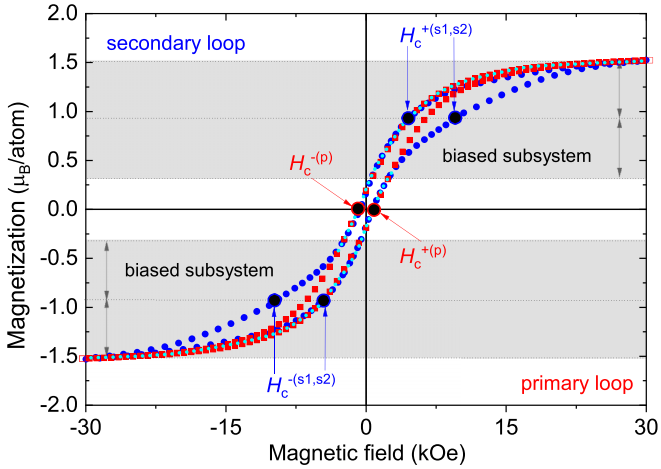

FIG. 10. Double hysteresis loop. Superimposition of the double hysteresis loops (DHLs) and primary loop at 50 K for $S1$. The blue arrows indicate the two coercive fields $H_c^{-(s1,s2)}$ at the bottom half and the other two $H_c^{+(s1,s2)}$ at the top half of the secondary loops (blue dotted line) as the system is broken into similar but two oppositely biased subsystems leading to a bidomain state. The red arrows indicate the usual two coercive fields $H_c^{\pm(p)}$ of the primary loop (red dotted line). Regions of the two subsystems along the y-axis are shown by the shaded gray regions at the top and down halves. The dotted cyan curves mark the overlapping regions.

in the presence of no magnetic field (ZFC). The magnetization $[M(T)]$ curves are shown in Figs. 15(a) and 15(b) for $S1$,

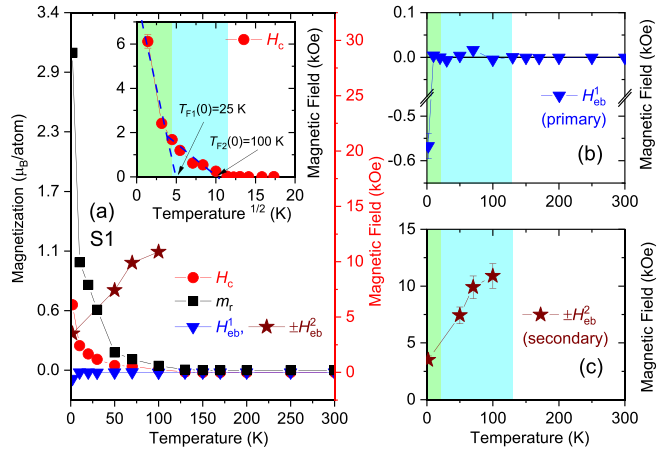

FIG. 11. m_r and H_c and H_{eb} for S1. (a) Remanent magnetization m_r, coercive field H_c, and exchange bias field H_{eb}^1 as a function of temperature. The inset shows H_c vs $T^{\frac{1}{2}}$ plot and its linear fit (blue dashed line) showing the maximum for the zero-field-cooled (ZFC) curves $T_{F1}(0) = 25$ K and $T_{F2}(0) = 100$ K. (b),(c) The plot of H_{eb}^1 and H_{eb}^2 vs temperature. The shaded regions mark the temperature ranges of helical (cyan) and conical (lime) phases for Ho in bulk.

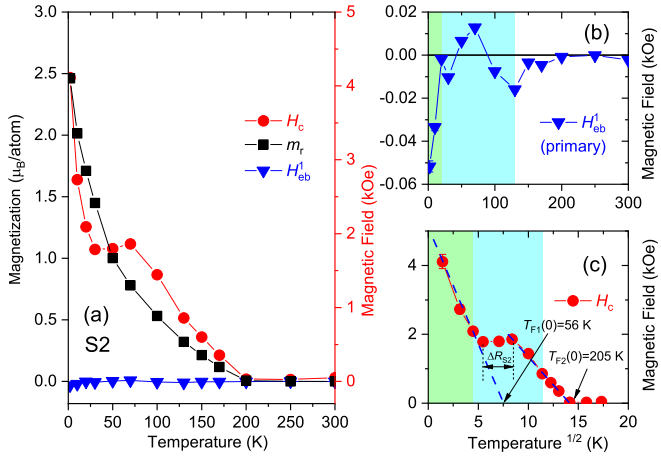

FIG. 12. m_r and H_c and H_{eb} for S2. (a) Remanent magnetization m_r, coercive field H_c, and exchange bias field H^1_{eb} as a function of temperature. (b) The plot of H^1_{eb} vs temperature. (c) The H_c vs $T^{\frac{1}{2}}$ plot and its linear fit (blue dashed line) showing the maximum for the zero field cooled (ZFC) curves $T_{F1}(0) = 56$ K and $T_{F2}(0) = 205$ K. The shaded regions mark the temperature ranges of helical (cyan) and conical (lime) phases for Ho in bulk.

Figs. 16(a) and 16(b) for $S2$, and Figs. 17(a) and 17(b) for $S3$ in various applied fields.

For $S1$ [Fig. 15(b)], we can see two peaks at $T_{F0} = 13$ K and $T_{F1} = 36$ K, which are around the temperature region of the conical phase of Ho with spin-flop characteristics. The presence of T_{F0} is a typical signature of the spin-flop characteristic. We also see a third peak $T_{F2} = 135$ K. Note that the basal plane component orders from a paramagnetic phase into a helical structure below 131 K. For $ML_{Tb} = 7$, as the Tb noncollinear spin configuration is poorly constituted, we do not find any peak associated with the Tb layers in $S1$ [16]. For $S2$ [Fig. 16(b)], one can see a peak $T_{F1} = 35$ K,

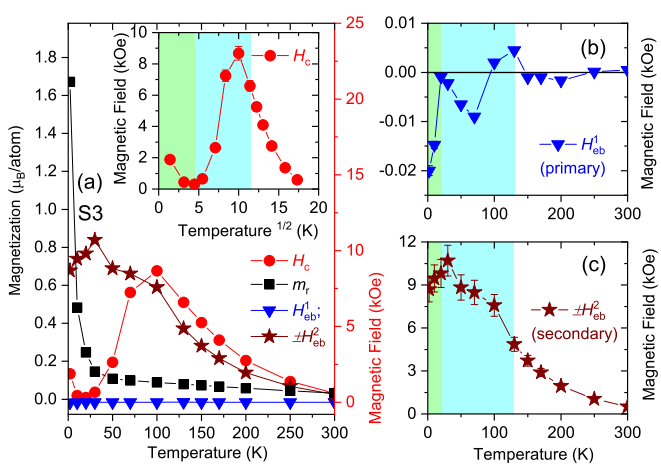

FIG. 13. m_r and H_c and H_{eb} for S3. (a) Remanent magnetization m_r, coercive field H_c, and exchange bias field H^1_{eb} as a function of temperature. The H_c vs $T^{\frac{1}{2}}$ plot is shown in the inset. (b),(c) The plot of H^1_{eb} on a zoomed-in plot and H^2_{eb} vs temperature. The shaded regions mark the temperature ranges of helical (cyan) and conical (lime) phases for Ho in bulk.

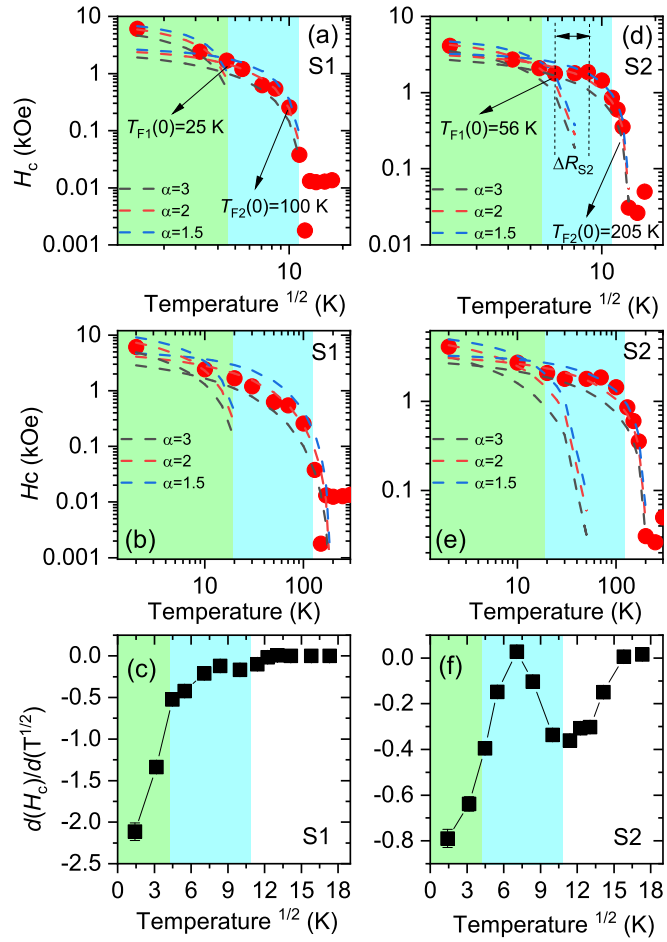

FIG. 14. Log-log plots of H_c and their derivatives vs temperature for $S1$ and $S2$. (a),(d) Coercive field H_c vs $T^{\frac{1}{2}}$; (b),(e) H_c vs T in log-log scales and their simulations for $\alpha = 3$ (black dashed line), 2 (red dashed line), and 1.5 (blue dashed line). $T_{F1}(0) = 25$ K; $T_{F2}(0) = 100$ K and $T_{F1}(0) = 56$ K; $T_{F2}(0) = 205$ K were used for simulating the two regimes of $S1$ and $S2$, respectively. (c),(f) The plots of the first derivative $d(H_c)/dT^{1/2}$ vs temperature $T^{1/2}$. The shaded regions mark the temperature ranges of helical (cyan) and conical (lime) phases for Ho in bulk.

which is around the temperature region of the conical phase of Ho, and a smaller peak at $T_{F2} = 127$ K, which is around the temperature region of the helical phase of Ho. Here also, for $ML_{Tb} = 21$, no peak can be related to Tb around the temperature of the helical phase of Tb (229–221 K).

Thus, following the magnetization versus temperature curves, no or little shift was observed in the two characteristic peaks $T_{F1,F2}$ at low-temperature ranges for $ML_{Tb} = 7$ and 21. The peaks for both samples were around 35–36 K (conical) and 127–135 K (helical). However, one may note that following the H_c versus $T^{1/2}$ plots for $ML_{Ho} = 7$ and 21 [insets of Figs. 11(a) and 12(a)], definitive shifts in both $T_{F1}(0)$ and $T_{F2}(0)$ were observed. These shifts indicate that the state of the helical phase formation in Tb, affecting the conical-to-helical and helical-to-paramagnetic phase fractions within Ho in Ho/Tb multilayers, is similar to that observed earlier in Er/Tb multilayers [17].

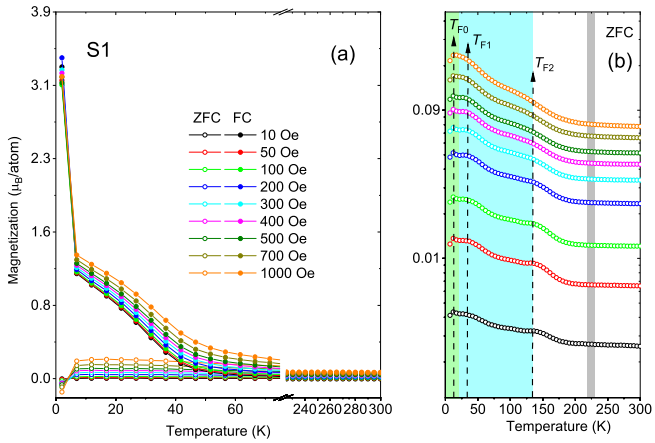

FIG. 15. FC-ZFC measurements for S1. (a) Temperature dependence of the dc magnetization. The measurements were done on heating at different fields after zero field cooling (ZFC) and field cooling (FC) in 70 kOe (7000 mT). (b) A maximum (at lower temperatures) for the zoomed-in ZFC curves ($T_{F0,F1,F2}$). The peak positions with increasing $\mathbf{H}_a$ are indicated by the dashed lines, which show no variation. The shaded regions mark the temperature ranges of helical (cyan) and conical (lime) phases for Ho and helical (gray) for Tb in bulk.

One may note that $T_{F0,F1,F2}$ are not influenced by the applied field for $S1$ and $S2$. For $ML_{Ho} = 29$, the turn angle is accumulated across $\approx$ 30 (3 × 10 ML below 40 K)/$\approx$28 (4 × 7 ML below 131 K) atomic layers of Ho, therefore the fraction of the spin noncollinear extension is limited. Moreover, no field-dependent convergence of the FC-ZFC curves can be ascertained for $S1$ or $S2$, although distinct divergences were observed.

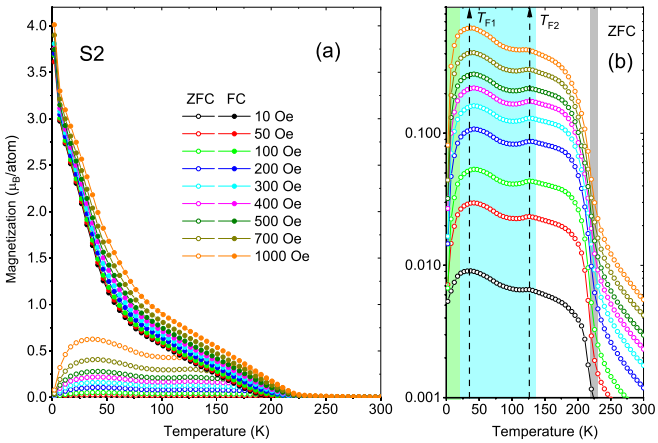

FIG. 16. FC-ZFC measurements for S2. (a) Temperature dependence of the dc magnetization. The measurements were done on heating at different fields after zero field cooling (ZFC) and field cooling (FC) in 70 kOe (7000 mT). (b) A maximum (at lower temperatures) for the zoomed-in ZFC curves ($T_{F0,F1}$). The peak positions with increasing $\mathbf{H}_a$ are indicated by the dashed lines, which show no variation. The shaded regions mark the temperature ranges of helical (cyan) and conical (lime) phases for Ho and helical (gray) for Tb in bulk.

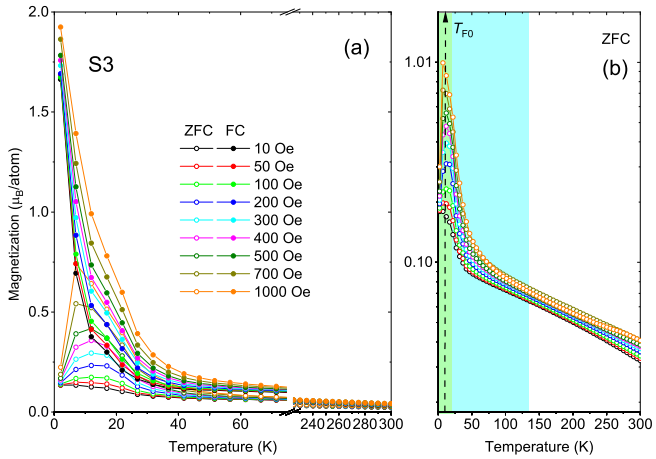

FIG. 17. FC-ZFC measurements for S3. (a) Temperature dependence of the dc magnetization. The measurements were done on heating at different fields after zero field cooling (ZFC) and field cooling (FC) in 70 kOe (7000 mT). (b) A maximum (at lower temperatures) for the zoomed-in ZFC curves (T_{F0}). The peak positions with increasing $\mathbf{H}_a$ are indicated by a dashed line, which shows no variation. The shaded regions mark the temperature ranges of helical (cyan) and conical (lime) phases for Ho in bulk.

Figures 18(a)–18(c) show the divergence of the FC-ZFC curves on a zoomed-in scale for $S1$, $S2$, and $S3$. The values of $T_{irr}^{S1} = 156$ K (above 300 Oe) and $T_{irr}^{S2} = 225$ K (above 50 Oe) are marked by dashed lines. Therefore, the irreversibility temperature T_{irr} shows no field dependence. The higher value of T_{irr}^{S2} can again be seen as an affect of higher Tb thickness. The divergence of ZFC and FC suggests some kind of magnetic frustration, which can be either due to the coexisting ferro (FM) and antiferromagnetic (AF) phases or due to noninteracting superparamagnetic particles. Magnetic coexistence is visible below 300 Oe (for $S1$) and 50 Oe (for $S2$) as the ZFC curves show higher values than the FC ones. For a purely

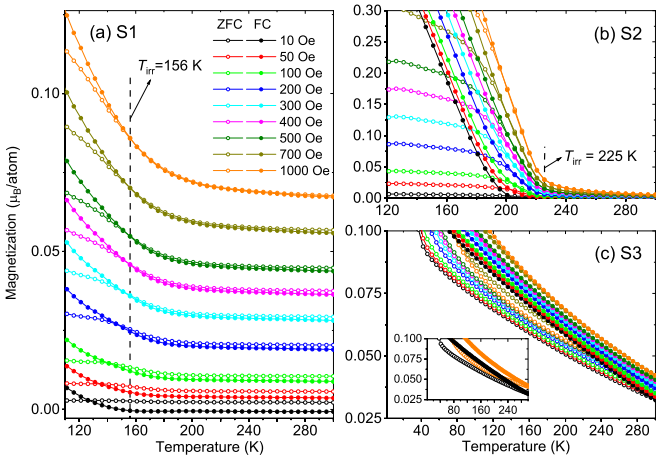

FIG. 18. Zoomed-in FC-ZFC measurements for $S1$, $S2$, and $S3$. Temperature dependence of the zoomed-in FC-ZFC curves showing the T_{irr} with increasing $\mathbf{H}_a$ for (a) $S1$, (b) $S21$, which are indicated by dashed lines, which show no variation. (c) For $S3$, the curves do not converge until at 300 K. The inset shows the nonconvergence of the curves for 10 Oe (1 mT) and 1000 Oe (100 mT).

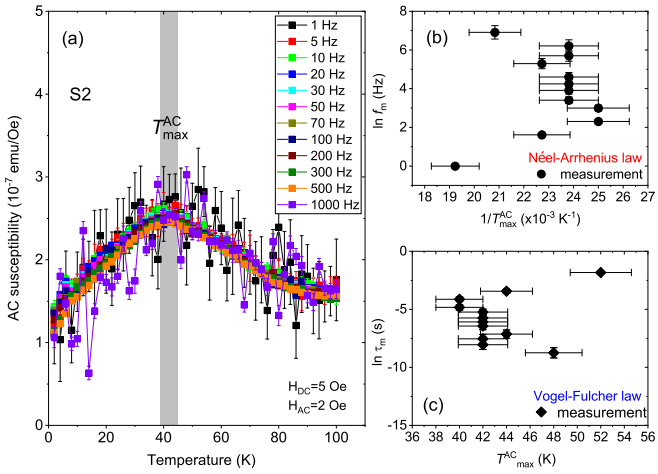

FIG. 19. ac measurements for $S2$. (a) The temperature dependence of the real part of the ac susceptibility [$\chi'(T)$] for frequencies ranging from 1 to 1000 Hz at a dc field of 5 Oe in $S2$. Frequency dependence of (b) T^{ac}_{max} plot for the Néel-Arrhenius model and the (c) Vogel-Fulcher model. The shaded region marks the range of T^{ac}_{max} in $S2$.

ferromagnetic transition, no thermomagnetic irreversibility is expected, whereas for a weak ferromagnet or a frustrated system with mixed FM and AF phases, irreversibility can be seen. Thus, $S1$ and $S2$ show typical FM behaviors within the low- and high-temperature regimes, and the peaks ($T_{F1,F2}$) are due to the mixed FM-AF phases in the system [16].

For $S3$, the FC-ZFC curves possess typical ferromagnetic behavior as shown in Fig. 17(b). We find $T_{F0} = 10$ K, which is a typical signature of the spin-flop process. Any possible nanoclustering behavior within Ho below 131 K is suppressed here by the presence of the FM (CoFe) layer. Note that the FC-ZFC curves do not converge before 300 K for $S3$ as shown in Fig. 18(c). The nonconvergence is exemplified in the inset of the figure for 10 Oe (1 mT) and 1000 Oe (100 mT).

3. ac susceptibilities

We perform a temperature dependence of the ac susceptibilities to negate the existence of nanoclustering behavior (which can be either SPM or SSG-type) in $S2$ and $S3$. One uses the frequency response of the peak in $\chi'(T)$ ($= d\mathbf{M}/d\mathbf{H}$) curves to probe different values of the relaxation time that categorizes the paramagnetic or glassy behaviors. We measure the ac responses over a frequency range of 1–1000 Hz in the presence of a small ac field of 2 Oe and a dc field of 5 Oe. The maxima in χ'(T) (T^{ac}_{max}), shaded in gray in Fig. 19(a), almost show no variation with frequency for $S2$. We also find no shift in T^{ac}_{max} for $S3$ (not shown).

One may note that no peak shift or unsystematic shift in T^{ac}_{max} would signify a standard FM behavior, whereas a systematic shift is expected for an archetypal SPM/SSG system. We qualitatively analyze the dynamical behavior using the Néel-Arrhenius law [33] and Vogel-Fulcher law [34], which are generally used to determine the relaxation time and plot the corresponding frequency behaviors of the ac magnetic susceptibility peak positions T^{ac}_{max} in Figs. 19(b) and 19(c). The unsystematic shift of T^{ac}_{max} as a function of frequency in $S2$ obviously does not comply with a typical SPM or SSG type of behavior. Such a behavior can therefore be attributed to regular FM behavior.

D. Exchange bias at the interfaces of Er/Tb and Ho/Tb multilayers

Interestingly, one may note that the exchange bias fields are approximately three times higher for $ML_{Tb} = 7$ interfaced with Ho (-0.57 ± 0.01 kOe) as compared to when interfaced with Er [17]. For the case reported earlier, the maximum exchange bias field for the $ML_{Tb} = 7$ sample was lower ($+0.17 \pm 0.01$ kOe) in the Er/Tb system. For the $ML_{Tb} = 21$ sample also, the maximum exchange bias has increased from $+0.013 \pm 0.01$ kOe in Er/Tb multilayers to -0.055 ± 0.01 kOe in Ho/Tb multilayers. Table I depicts the different parameters extracted from the magnetization measurements.

In both multilayers Er/Tb and Ho/Tb, from the H_c versus temperature curves, we find shifts in the two temperature regimes of magnetic behaviors related to the conical-to-helical ($T_{F1(0)}$) and helical-to-sinusoidal (Er) or helical-to-paramagnetic (Ho) phases ($T_{F2(0)}$), respectively. However, we find the transition phase ($\Delta R_{S2} \approx 42$ K) exists only for the Ho/Tb system for a similar number of MLs ($ML_{Tb} = 21$). Note that such a transition phase was reported for the Er/Tb

TABLE I. Parameters extracted from the magnetization measurements. The columns indicate the conical (marked in lime) and helical (marked in cyan) phases in Ho (Er), while those marked in gray indicate the range of helical phase in Tb.

Multilayer	d_{Tb} (nm/MLs)	$T_{F1(0)}$ (K)	$T_{F2(0)}$ (K)	ΔR (K)	T_{F0} (K)	T_{F1} (K)	T_{F2} (K)	T_{F3} (K)	T_{irr} (K)	H^1_{eb} (kOe)
$[Er_x\|Tb_y]_{\times 10}$; x, y = number of ML										
$[Er_{21}\|Tb_5]$ [17]	1.5/5	56	150		7	26	50			0.17 ± 0.01 (5 K)
$[Er_{21}\|Tb_{21}]$ [17]	6.0/21	72	196			35	100–150	200		0.013 ± 0.005 (2 K)
$[Er_{36}\|Tb_{35}]$ [16]	10.0/35	64	200	70		37		204	210 (100 Oe)	-0.011 ± 0.01 (5 K)
$[Ho_x\|Tb_y]_{\times 10}$; x, y = number of ML										
$[Ho_{29}\|Tb_7]$: $S1$	2.0/7	25	100		13	36	134		156 (300 Oe)	-0.57 ± 0.01 (2 K)
$[Ho_{29}\|Tb_{21}]$: $S2$	6.0/21	56	205	42		35	127		225 (50 Oe)	-0.055 ± 0.005 (2 K)

system also ($\Delta R_{\mathrm{Er/Tb}} \approx 70$ K), but only for the sample with a higher number of MLs ($\mathrm{ML_{Tb}} = 35$) [16]. This indicates the increased significance of the Tb spin-spiral affecting the Ho/Tb spin configurations as compared to that affecting the Er/Tb spin configurations. Note that the Tb moments are affecting the Ho (or Er) spin configurations at temperatures where they are expected to be in the purely FM phase. Furthermore, no significant temperature variation of the characteristic peaks in the ZFC curves and the effect of applied fields are seen for both systems. Also, both systems show typical FM behavior from the ac susceptibility measurements.

The overall increase in the bias fields can be attributed to the increased number of spin imbalances in Ho as compared to Er. The stabilized conical structure exists in both Ho and Er, but the cone angle between the *c*-axis and the moments at 4 K is large (about 80°) in Ho and small (about 30°) in Er [18]. The uniaxial anisotropy of Er, $K_{\mathrm{u}}^{\mathrm{Er}} \sim -1.9 \times 10^7$ J/m^3, is usually two orders of magnitude higher than the basal plane anisotropy ($K_{\mathrm{b}}^{\mathrm{Er}} \sim \times 10^5$ J/m^3 at 4 K [35]). However, for Ho, the two anisotropies are comparable as $K_{\mathrm{u}}^{\mathrm{Ho}} \sim 2.5 \times 10^6$ J/m^3 [36]. Due to the large hexagonal anisotropy in Ho, the turn angle between the moments in successive planes averages 30° in the temperature range of the helix, while they are confined to the *a*-*c* plane for Er in the helical temperature range. Thus, the angle that each magnetic sublattice plane subtends with the next is lower in Er than in Ho, which can contribute more to the sublattice disorder during the field-cooling process in Ho.

IV. SUMMARY AND CONCLUSION

In this work, we report on the magnetic properties of Ho-Tb interfaces of high-textured grown multilayers for two different Tb thicknesses representing commensurable structures for different MLs with $\mathrm{ML_{Ho}} = 29$, and $\mathrm{ML_{Tb}} = 7$ and 21. The different individual thicknesses are used to explore the effect of the fraction of the noncollinear spin configuration of Tb on the conical-to-helical phases within Ho as a function of temperature.

Significant exchange bias coupling (up to $H_{\mathrm{eb}} = -0.57$ kOe) around the temperature below 20 K or in the range of the conical phase of Ho was observed for $\mathrm{ML_{Tb}} = 7$, which decreases significantly for higher temperatures of the helical phase of Ho. Very low or insignificant exchange bias of up to –0.055 kOe was observed for $\mathrm{ML_{Tb}} = 21$.

Analysis of the H_{c} versus temperature curves indicates two different magnetic behavior regimes ($\Delta r_{S1}^1 = 16$ K and $\Delta r_{S2}^1 = 56$ K; $\Delta r_{S1}^2 = 84$ K and $\Delta r_{S2}^2 = 136$ K), one related to the conical-to-helical phase and the other to the helical-to-paramagnetic phase in Ho, which shifts to higher temperatures for increased number of Tb MLs ($\mathrm{ML_{Tb}} = 21$). However, no shift was observed in the two characteristic peaks ($T_{\mathrm{F1,F2}}$) around low-temperature ranges of 35 and 130 K, which are similar to that of the conical and helical phases of Ho, respectively. Additionally, ac frequency-responsive behavior, which does not comply with the SPM/SSG-type of characteristics, is observed around the low-temperature range (20–60 K), at least for the $\mathrm{ML_{Tb}} = 21$ sample.

Small statistical spin-imbalance in the number of magnetic sublattice disorders leads to irreversible moments in RE contributing to such exchange bias fields relevant for the noncollinear configuration or conical phase of Ho. Replacing Tb with CoFe in Ho/CoFe multilayers, we observe usual DHLs and substantial negative exchange bias as observed earlier for other FM-RE systems.

ACKNOWLEDGMENTS

We would like to thank Electron Microscopy Center at the GTIIT for TEM measurements. X.X., K.Z., and Y.C. did the sample preparation, magnetization, and the TEM measurements supervised by A.P. The data treatment for the magnetization measurements was done by X.X., K.Z., Y.C., H.L., Y.W., and S.Y. under the supervision of A.P. All authors reviewed the manuscript. A.P. conceived and designed the work, analyzed the data, coordinated the work, and wrote the manuscript.

The authors declare no competing interests.

[1] C. F. Majkrzak, J. Kwo, M. Hong, Y. Yafet, D. Gibbs, C. L. Chien, and J. Bohr, Magnetic rare earth superlattices, Adv. Phys. **40**, 99 (1991).

[2] R. A Cowley, Magnetic structures and coherence of rare earth superlattices, Phys. B: Condens. Matter **350**, 1 (2004).

[3] R. A. Cowley, The coherence of the magnetic structures of rare-earth superlattices, J. Magn. Magn. Mater. **177–181**, 1156 (1998).

[4] J. P. Goff, Rare-earth thin films and superlattices, J. Phys.: Condens. Matter **32**, 374009 (2020).

[5] D. A. Jehan, D. F. McMorrow, R. A. Cowley, R. C. C. Ward, M. R. Wells, N. Hagmann, and K. N. Clausen, Magnetic structure of holmium-yttrium superlattices, Phys. Rev. B **48**, 5594 (1993).

[6] C. de la Fuente, R. A. Cowley, J. P. Goff, R. C. C. Ward, M. R. Wells, and D. F. McMorrow, The magnetic structures of holmium-yttrium superlattices in an applied magnetic field, J. Phys.: Condens. Matter **11**, 6529 (1999).

[7] V. V. Tarnavich, D. Lott, S. Mattauch, A. Oleshkevych, V. Kapaklis, and S. V. Grigoriev, Field-induced chirality in the helix structure of Ho/Y multilayers, Phys. Rev. B **89**, 054406 (2014).

[8] V. Tarnavich, E. Tartakovskaya, Yu. Chetverikov, V. Golub, D. Lott, Yu. Chernenkov, A. Devishvili, V. Ukleev, V. Kapaklis, A. Oleshkevych, V. Fedorov, V. Bairamukov, A. Vorobiev, and S. Grigoriev, Magnetic field induced chirality in Ho/Y multilayers with gradually decreasing anisotropy, Phys. Rev. B **96**, 014415 (2017).

[9] C. Dufour, K. Dumesnil, and P. H. Mangin, Strain-induced modification of magnetic structure and new magnetic phases in rare-earth epitaxial films, Pramana - J. Phys. **67**, 173 (2006).

[10] C. Bryn-Jacobsen, R. A. Cowley, D. F. McMorrow, J. P. Goff, R. C. C. Ward, and M. R. Wells, Coherent magnetic

structures in terbium/holmium superlattices, Phys. Rev. B **55**, 14360 (1997).

[11] A. Paul, S. Mukherjee, W. Kreuzpaintner, and P. Böni, Exchange-bias-like coupling in a ferrimagnetic multilayer Fe-Tb, Phys. Rev. B **89**, 144415 (2014).

[12] S. Mukherjee, W. Kreuzpaintner, J. Stahn, J.-G. Zheng, A. Bauer, P. Böni, and A. Paul, Exchange-bias-like coupling in a Cu-diluted-Fe-Tb multilayer, Phys. Rev. B **91**, 104419 (2015).

[13] S. Fust, S. Mukherjee, N. Paul, J. Stahn, W. Kreuzpaintner, P. Böni, and A. Paul, Realizing topological stability of magnetic helices in exchange coupled multilayers for all-spinbased system, Sci. Rep. **6**, 33986 (2016).

[14] J. Ye, T. Baldauf, S. Mattauch, N. Paul, and A. Paul, Topologically stable helices in exchange coupled rare-earth/rare-earth multilayer with superspin-glass like ordering, Commun. Phys. **2**, 114 (2019).

[15] S. Jenkins, W. J. Fan, R. Gaina, R. W. Chantrell, T. Klemmer, and R. F. L. Evans, The atomistic origin of exchange anisotropy in non-collinear IrMn/CoFe, Phys. Rev. B **102**, 140404(R) (2020).

[16] J. Huang, C. Liu, B. Yuan, X. Xiao, and A. Paul, Exchange coupling due to spin-imbalance in Er magnetic sublattice within Er/Tb multilayers, J. Magn. Magn. Mater. **585**, 171108 (2023).

[17] X. Xiao, K. Zhao, Y. Cui, J. Chen, J. Liao, B. Du, and A. Paul, Exchange coupling at the interfaces of Er/Tb and Er/CoFe multilayers, J. Phys. Chem. C **127**, 20549 (2023).

[18] J. Jensen and A. R. Mackintosh, *Rare Earth Magnetism: Structures and Excitations* (Clarendon Press, Oxford, 1991).

[19] T. Kosugi, S. Kawano, N. Achiwa, A. Onodera, Y. Nakai, and N. Yamamoto, Direct evidence of helifan structures in holmium by single crystal neutron diffraction, Phys. B: Condens. Matter **334**, 365 (2003).

[20] A. Paul, Stiffness in vortex-like structures due to chirality-domains within a coupled helical rare-earth superlattice, Sci. Rep. **6**, 19315 (2016).

[21] J. Kwo, M. Hong, and S. Nakahara, Growth of rare-earth single crystals by molecular beam epitaxy: The epitaxial relationship between hcp rare earth and bcc niobium, Appl. Phys. Lett. **49**, 319 (1986).

[22] J. Yu, Exploring the magnetic phases in dysprosium by neutron scattering techniques, Ph.D. thesis, University of Alabama, 2014.

[23] A. R. Wildes, J. Mayer, and K. Theis-Bröhl, The growth and structure of epitaxial niobium on sapphire, Thin Solid Films **401**, 7 (2001).

[24] D. I. Devyaterikov, E. A. Kravtsov, V. V. Proglyado, V. D. Zhaketov, and Yu. V. Nikitenko, Investigation of Helimagnetism in Dy and Ho thin films by neutron reflectometry, J. Surf. Investig. **15**, 542 (2021).

[25] K. Mašek and V. Matolín, RHEED study of Nb thin film growth on α-Al_2O_3 (0001) substrate, Thin Solid Films **317**, 183 (1998).

[26] J. A. Borchers, M. B. Salamon, R. W. Erwin, J. J. Rhyne, R. R. Du, and C. P. Flynn, Structural and magnetic properties of Er thin films and Er/Y superlattices: Magnetoelastic effects, Phys. Rev. B **43**, 3123 (1991).

[27] G. Liu, X-ray diffraction from thin film structures: characterization and modeling, Ph.D. thesis, University of California, 2007.

[28] M. Holtschneider and W. Selke, Uniaxially anisotropic antiferromagnets in a field on a squarelattice, Eur. Phys. J. B **62**, 147 (2008).

[29] X. Xiao, K. Zhao, Y. Cui, B. Yuan, V. V. Jadhav, and A. Paul, Spin-flop process identified in heteroepitaxial rare-earth films of Er and Ho, Appl. Phys. Lett. **124**, 142401 (2024).

[30] M. Kiwi, J. Mejía-Lopéz, R. D. Portugal, and R. Ramírez, Positive exchange bias model: Fe/FeF_2 and Fe/MnF_2 bilayers, Solid State Commun. **116**, 315 (2000).

[31] A. Paul, N. Paul, P. Müller-Buschbaum, A. Bauer, and P. Böni, Superparamagnetic regular nanopillar-like structures studied by grazing-incidence X-ray scattering: effect of vertical correlation, J. Appl. Cryst. **47**, 1065 (2014).

[32] M. Knobel, W. C. Nunes, L. M. Socolovsky, E. De Biasi, J. M. Vargas, and J. C. Denardin, Superparamagnetism and other magnetic features in granular materials: A review on ideal and real systems, J. Nanosci. Nanotechnol. **8**, 2836 (2008).

[33] L. Néel, Théorie du traînage magnétique des ferromagnétiques en grains fins avec application aux terres cuites, Ann. Géophys. **5**, 99 (1949).

[34] H. Vogel, The law of temperature dependence of the viscosity of fluids, Phys. Z. **22**, 645 (1921).

[35] P. De. V. Du Plessis, Magnetic anisotropy of some heavy rare-earth metals, Physica **41**, 379 (1969).

[36] Yu. S. Vishnyakov, V. L. Ivannikov, R. Z. Levitin, and B. K. Ponomarev, Determination of the magnetic uniaxial anisotropy constants of holmium from magnetization measurements in fields up to 240 kOe, Zh. Eksp. Teor. Fiz. **57**, 1956 (1969) [Sov. Phys. JETP **30**, 1059 (1970)].